Research Article

Xiangmiao Zhu, Weitong Qi, Mi Wang, Shixuan Zhan, Xuezhao Liu, Yuting Zhao,
Volker Hessel, Zhanghao Chen, and Liangliang Lin*

Microfluidic steam-based synthesis of luminescent carbon quantum dots as sensing probes for nitrite detection

https://doi.org/10.1515/gps-2022-8144
received November 27, 2022; accepted April 04, 2023

Abstract: In this work, an efficient and green approach has been presented to prepare carbon quantum dots (CQDs) from watermelon juice through a microfluidic steam-based method, with a view to enabling continuous production at scale, i.e., to save time, costs, or energy as compared to conventional production using an autoclave. The evolution of the product formation through multifarious intermediates generated in different stages of the reaction process was characterized. Computational fluid dynamics simulations reveal the pressure and velocity profiles in the microchannel to exert process control. These determine the quality of the obtained CQDs by influencing the particle size transformations and manifold chemicals along the microchannel axis. The optimal reaction conditions and reaction mechanism for the synthesis of CQDs were investigated. Additionally, the synthesized CQDs demonstrated good fluorescence properties as well as a specific response to NO_2^- in both fluorescence and spectrophotometric modes, providing great potential for their application in environmental monitoring.

Keywords: carbon quantum dots, microreactor, flow synthesis, nitrite detection

1 Introduction

As a new “zero-dimensional” carbon nanomaterial, carbon quantum dots (CQDs) have attracted widespread attention because of their tunable fluorescence property, outstanding stability, photobleaching resistance, and excellent biocompatibility [1,2]. A wide range of biomass precursors, including watermelon juice, orange juice, soy milk, etc., have been exploited to prepare CQDs [3,4], which show promising applications in different areas, such as chemical sensors, bioimaging probes, photocatalysts, light-emitting diode, and drug delivery [5].

With increasing environmental awareness, many studies have been devoted to applying CQDs for environmental monitoring [6,7]. For instance, nitrite commonly exists in food or cosmetics but can form nitrosamine compounds due to improper processing. Most of these compounds were carcinogenic in animal tests. Since nitrite can react with the amide/amine groups on the surfaces of N-CDs to cause fluorescence quenching, Jia et al. [8] successfully designed a CQD-based probe for the detection of nitrite. Another example was reported by Wu et al. [9], where CQDs and nitrite were mixed in the presence of 3-aminophenol (3-Aph) to yield a yellow-colored azoic compound and gave the colorimetric readout. Despite remarkable progress being achieved in the application of CQDs, these synthetic methods are batch processing and require tedious operational procedures and large amounts of solvent. This together with their poor uniformity and unavoidable residues may deteriorate the fluorescence properties and limit their applications [10,11]. Thus, it is urgent to develop a method for the synthesis of CQDs with good fluorescence performance in a simple and green manner.

*** Corresponding author: Liangliang Lin,** School of Chemical and Material Engineering, Jiangnan University, Wuxi 214122, China; The Key Laboratory of Synthetic and Biological Colloids, Ministry of Education, Jiangnan University, Wuxi 214122, China, e-mail: linliangliang@jiangnan.edu.cn

Xiangmiao Zhu: School of Chemical and Material Engineering, Jiangnan University, Wuxi 214122, China; The Key Laboratory of Synthetic and Biological Colloids, Ministry of Education, Jiangnan University, Wuxi 214122, China

Weitong Qi, Mi Wang, Shixuan Zhan, Xuezhao Liu, Yuting Zhao: School of Chemical and Material Engineering, Jiangnan University, Wuxi 214122, China

Volker Hessel: School of Chemical Engineering and Advanced Materials, The University of Adelaide, North Terrace Campus, Adelaide 5005, Australia

Zhanghao Chen: Guangdong Institute for Drug Control, NMPA Key Laboratory for Safety Risk Assessment of Cosmetics, Guangzhou 510180, China

As an emerging technique for nanomaterial synthesis, microfluidic technology has been widely applied in the efficient synthesis of quantum dots, metal particles, metal–organic skeleton materials, nano-zeolite, and other nanomaterials due to its microfluidic channel structure of the order of microns, excellent droplet and flow mode control performance, and fast heat and mass transfer, which can significantly decrease [12] costs and time of production as well as precursor consumption [13,14]. The improvements that microreactors have brought in several reactions over conventional reactors are shown in Table 1.

In this work, a microfluidic system was established, which consisted of syringe pumps, a capillary microreactor, an oil bath, and a condensation collection device. With this system, CQDs were first prepared by a simple and efficient microfluidic steam-based method from biomass precursors, with the motivation to demonstrate a novel and green way for the production of luminescent CQDs. The characterization results of CQDs not only provide information about their performance, such as fluorescence property, particle size distribution, and crystal geometry, but also show the differences among intermediate products, which preliminarily prove the reaction progress. To fully exploit the potential of microfluidics and further develop a robust and at-scale process, it is needed to understand the formation mechanism of CQDs in the microreactor. Thus, computational fluid dynamics (CFD) simulation was utilized in conjunction with advanced products' characterization to dig into the reaction process. Furthermore, relying on their high selectivity and sensitivity for nitrite detection, CQDs were used as sensing probes for environmental analysis.

2 Materials and methods

2.1 Materials and instruments

The watermelon juice (absolutely pulp-free) was fresh-squeezed from the watermelon, which was purchased from the local market (Wuxi, China). Chemical agents (NaCl, $Co(NO_3)_2{\cdot}6H_2O$, $Ni(NO_3)_2{\cdot}6H_2O$, $HgCl_2$, $CuCl_2{\cdot}2H_2O$, $ZnCl_2$, $FeCl_3$, $Cr(NO_3)_3{\cdot}9H_2O$, NH_4F, KBr, KI, $NaNO_3$, $NaNO_2$, Na_2CO_3, $PbSO_4$, and Na_3PO_4) were purchased from Sinopharm Chemical Reagent Co., Ltd. (Shanghai, China). Deionized water was employed throughout all experiments.

The size and shape of CQDs were characterized using a JEOL JEM-2100 plus transmission electron microscope (TEM) operated at 200 kV. The photoluminescence properties and UV/Vis absorption spectra were recorded with a CARY Eclipse spectrophotometer (Varian, USA) and a TU-1950 spectrophotometer (Persee, China), respectively. The Fourier transform infrared spectra (FT-IR) of CQDs were recorded with a Nicolet 6700 spectrometer (Thermo Fisher, USA) ranging from 600 to 4,000 cm^{-1}. X-ray diffraction (XRD) was performed using a D8 (AXS Bruker, Germany) diffractometer with a mono X-ray source Cu Kα excitation (40 kV) and a Lynxeye array detector. Dynamic light scattering (DLS) was measured using a ZetaPALS instrument (Brookhaven, USA). Fluorescence decay curves were measured by a Lifespec ll ultrafast time-resolved fluorescent lifetime spectrometer (Edinburgh Instruments, UK).

2.2 Synthesis of CQDs

A total of 30 mL of fresh-squeezed watermelon juice was injected into a capillary microreactor (length = 3 m, inner diameter = 1 mm) by a syringe pump, of which the flow rates were set at 0.234, 0.078, 0.026, and 0.0196 $mL{\cdot}min^{-1}$, respectively. The temperature of the oil bath was maintained constant at 130°C. After a certain reaction time, the CQDs were pushed out by steam and collected by condensation. The obtained CQD solution was then dialyzed against water (MW cutoff: 500 Da) for 24 h to achieve purification.

2.3 CFD analysis

CFD analysis is an effective way to calculate the process parameters, such as pressure, temperature, and flow rate.

Table 1: Results of several reactions in microreactors compared with conventional reactors

Reaction	Reactor	Residence time	Temperature (°C)	Yield (%)
1. Substitution reaction of trimethyl phenylborate [13]	Flask	22 min	20	85.1
	Microreactor	5 s	20	98.9
2. Transesterification of ethyl butyrate [14]	Slurry reactor	30 min	60	87
	Microreactor	4 min	60	~95
3. Heck aminocarbonylation in $PdCl_2$(dppp) [15]	Flask	10 min	80	25
	Microreactor	2 min	80	55

It has been applied to solve numerous research and engineering problems in many fields, including aerodynamics and aerospace analysis, weather simulation, fluid flows, and heat transfer processes. In this study, CFD analysis was carried out with COMSOL software. To choose the right flow conditions, the Reynolds number (Re) should be determined first. Re is used to predict flow patterns in fluids, where the Re ranges divide transporting into three regimes: laminar, transitional, and turbulent. Low Re values correspond to laminar flow, whereas high Re values describe turbulent flow [15,16]. This dimensionless unit is a ratio of the inertial force to the viscous force:

$$\mathrm{Re} = \rho V D/\mu \tag{1}$$

Low density (ρ, $\mathrm{kg{\cdot}m^{-3}}$), flow rates (V, $\mathrm{m{\cdot}s^{-1}}$), viscous liquids (high μ, Pa·s), and small channels diameter (D, m) generally produce laminar flow ($\mathrm{Re} < 2{,}040$), with the range $\mathrm{Re} < 1{,}000$ being called truly laminar and $1{,}000 < \mathrm{Re} < 2{,}040$ being transitional. Typically, micro-flow liquids in microreactors are laminar. In addition, we assumed that the temperature of the inner wall of the microchannel is constant and the entire system does not involve heat exchange.

2.4 Detection of NO_2^- using CQDs

The as-prepared CQD solution ($1.50\ \mathrm{mg{\cdot}mL^{-1}}$) was diluted with deionized water. Various concentrations of $NaNO_2$ were separately added into the above diluted CQD solution. The resulting solutions were recorded for their emission spectra at 470 nm and absorbance values at 295 and 540 nm. The selectivity of CQDs to NO_2^- was investigated by adding different anions or metal ion stock solutions instead of NO_2^- in the same way.

3 Results and discussion

3.1 CFD analysis of the pressure and velocity profiles in the microchannel

The defined setting of the phase state of the reaction medium is crucial for the outcome of the reaction. Suppose that the liquid phase is followed by the gas phase in the microchannel, as shown in Scheme 1.

The expected phase setting requires knowledge and control of the pressure and velocity profiles in the microchannel. Specifically, these determine the quality of the CQD nanoproducts, which is required to influence, in a gross, overarching manner, the manifold chemical and particle size transformations along the microchannel axis. This motivation guides the CFD investigations as follows.

Scheme 1 shows that, at position 0, the inlet flow changes by evaporation from liquid to gas at a pressure P_0. If the above assumption holds, P_0 is equal to the saturated vapor pressure of water at that temperature. Position L is the outlet, where the pressure (PL) is easy to measure. The static pressure energy of the compressible fluid flowing in the straight pipe decreases, since one part of it is used to increase the kinetic energy of fluid expansion, and another part is used to overcome the frictional resistance loss. The kinetic energy conservation for steam transmission can be estimated by the following formula:

$$\mathrm{d}\left(\frac{u^2}{2}\right) = -\frac{\mathrm{d}P}{\rho} - \lambda \cdot \frac{\mathrm{d}u}{D} \cdot \frac{u^2}{2} \tag{2}$$

which is based on the principle of conservation of mass and momentum, derived from the basic differential

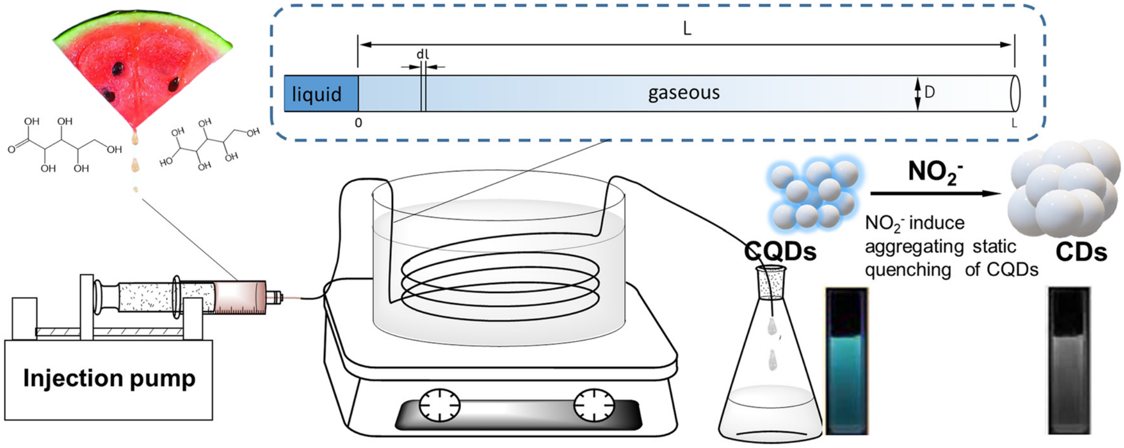

Scheme 1: Illustration of the synthetic procedure of CQDs and their sensing mechanism for the detection of NO_2^-.

equation of the compressible fluid in a tube. In Eq. 2, P (Pa) is the pressure, ρ (kg·m^{-3}) is the density, and D (m) is the pipe diameter. Because the gas density is small, its potential energy change ($g{\cdot}dz$) can be ignored. u can be replaced by the mass flow rate (G, g·s^{-1}) and axial velocity (v, m·s^{-1}) and then the above formula can be rewritten as follows:

$$G^2\ln\frac{v_L}{v_0} + \int_{P_0}^{P_L}\frac{dP}{v} + \frac{\lambda G^2 L}{2D} = 0 \qquad (3)$$

This simplifies further to

$$P_0 - P_L = \frac{2G^2}{P_0 + P_L}\left(\ln\frac{P_0}{P_L} + \frac{\lambda L}{2D}\right)\cdot\frac{RT}{M} \qquad (4)$$

where M is the molecular weight of steam, R (=8.314 J·mol^{-1}·K^{-1}) is the universal gas constant, and T (K) is the temperature. When $G = 4.3 \times 10^{-4}$ g·s^{-1} and $T = 403.15$ K, the P_0 of the solution is almost equal to P_L. Therefore, the variation in the fluid expansion kinetic energy is minimal, and the first term in the bracket on the right-hand side of Eq. 4 can be ignored, which is consistent with the Bernoulli equation [17] for incompressible fluid flowing in a straight horizontal pipe.

When P_0 is much smaller than the saturated vapor pressure (2.66×10^5 Pa) of water vapor at 403.15 K, the above assumption does not hold and the quantum dot precursor would only be exposed to the gaseous reaction medium. The precursor residence times in the microreactor are 0.33, 1, 3, and 4 s and correspond to the volume flow rates (u) of 0.234, 0.078, 0.026, and 0.0196 mL·min^{-1}, respectively.

Based on the above calculations, the whole flow process was simulated as shown in Scheme 2. Considering a reaction temperature of 130°C and a residence time of 4 s as an example, the gas in the microchannel has the following characteristics: isobaric at any position; the flow velocity only depends on the distance from the center of the channel cross section; and the greater the distance, the smaller the flow velocity and v_{Max} is 1.71 m·s^{-1}.

3.2 Characterization

In order to study the mechanism of the microfluidic method for the CQD synthesis, the process temperature and process time have to be considered. As shown in Scheme 1, the fluorescence intensity of the as-prepared CQD initially increased at a temperature of 110°C to 130°C and showed the strongest PL intensity at 130°C. After that, the fluorescence intensity decreased with a further increase of temperature (Figure A1 in the Appendix). This is ascribed to the generation of increasing carbon nuclei, where the fluorescence intensity of CQDs increased with the temperature accordingly. As the process temperature further increased, the size of CQDs gradually increased and became uneven (Figure A2), leading to a decrease in the fluorescence intensity [18].

FT-IR, UV/Vis absorption, and PL spectra as well as the XRD pattern reveal clearly the transformation of the functional groups in the molecules of the juice, the generation of carbon nucleus crystal planes, and the fluorescence effect along the duration of the heating process. FT-IR spectra of CQDs are displayed in Figure 1a, revealing the presence of peaks at 3,350, 2,950, 1,680, 1,410, and 1,100 cm^{-1}. They are assigned to the stretching vibrations of ν(OH), ν(C–H), ν(C=C), δ(C–N), and ν(C–O), respectively. This demonstrates that CQDs have plentiful functional groups, such as hydroxyl, amide, and/or amino. Two peaks at 1,720 and 1,220 cm^{-1} only appear on the FT-IR spectrum of CQDs synthesized at a process time of 0.33 s, corresponding to ν(C=O) and ν_{as}(C–O–C). Therefore, at a residence time of more than 1 s, the carboxyl groups are mostly carbonized into carbon bonds.

Figure 1b and c shows the absorption and excitation/emission profiles recorded for CQDs at four different

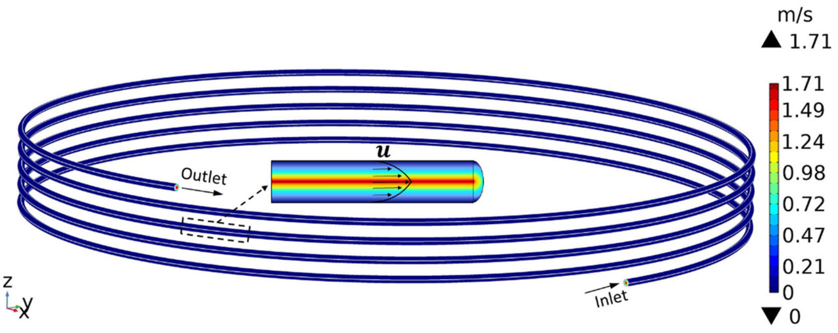

Scheme 2: The simulated results of velocity distribution in the microchannel.

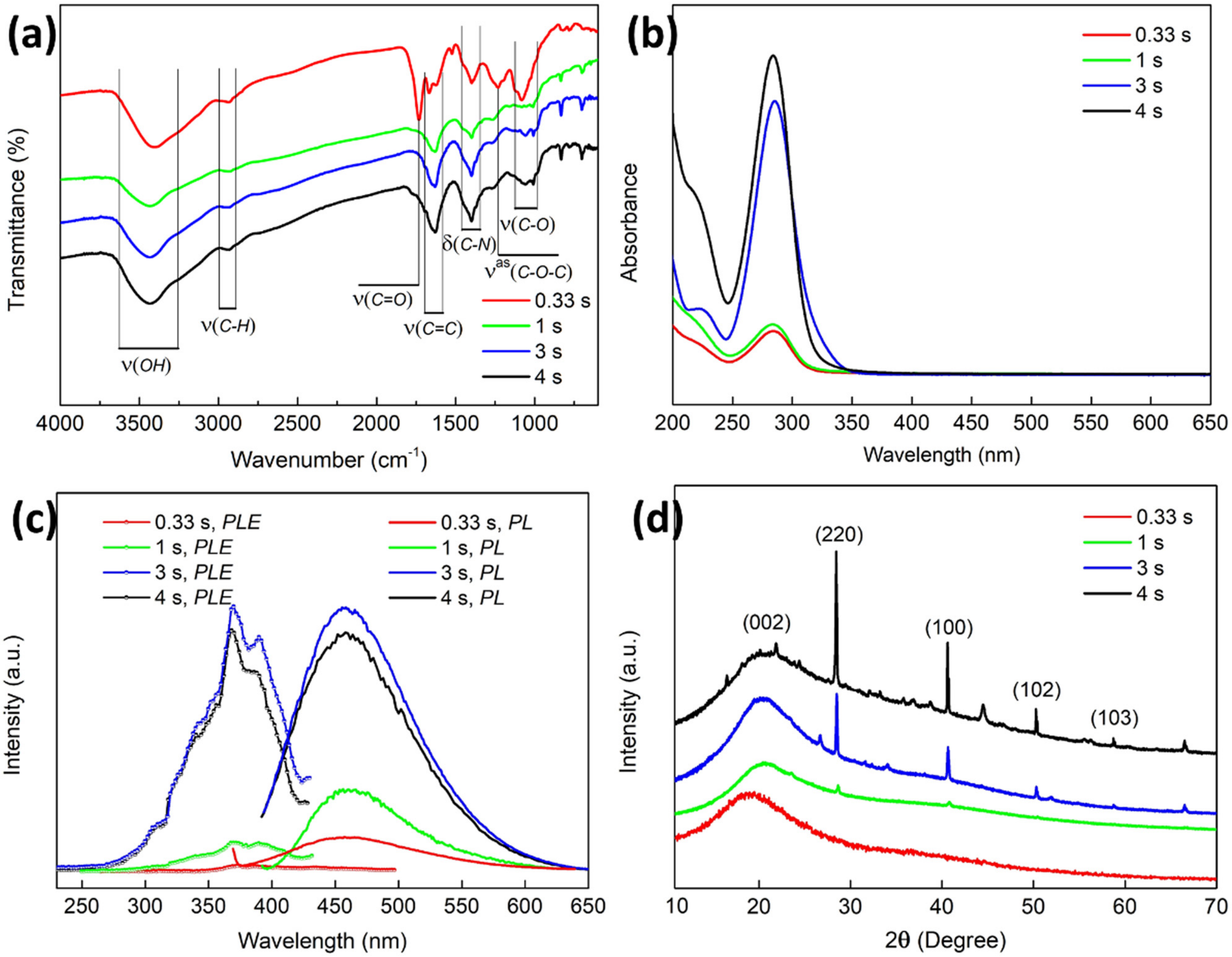

Figure 1: The FT-IR (a), UV/Vis absorption (b), fluorescence spectra (c), and XRD pattern (d) of CQDs prepared from watermelon juice by a microfluidic method at different process times and 130°C.

residence times. The UV/Vis absorption profile of the CQDs exhibits a narrow band at 285 nm, which is attributed to the presence of aromatic π–π* transition [8]. However, in the PLE/PL spectrum, we found that, when excited with 370 nm incident light, CQDs show a strong peak around 470 nm, which is ascribed to band gap transition corresponding to conjugated π-domain and surface defects present in the quantum dots [19]. In addition, the prolongation of the reaction time leads to an increase in the yield of CQDs and the degree of carbonization, resulting in an increase in the UV/Vis absorption intensity and fluorescence property of CQDs. A decrease in the fluorescence intensity is observed after a process time of more than 3 s, as the carbonization degree of CQDs increases, the defect states decrease, the non-radiative recombination process is inhibited, and the fluorescence is mainly derived from the eigenstate [20].

The XRD patterns of CQDs shown in Figure 1d revealed distinct Bragg peaks located at diffraction angles (2*θ*) of ~20°, 28.48°, 40.62°, 50.34°, and 58.72°, corresponding to the {002}, {220}, {100}, {102}, and {103} planes, respectively. The first four facets originate from graphitic (sp^2) carbon and the last one is from diamond-like (sp^3) carbon [21,22]. The peak of {002} facets centered at 19.2° in the CQDs synthesized in 0.33 s has been shifted to 20.9° in the case of CQDs with residence time of 3 s, corresponding to the lattice spacing from 0.46 to 0.42 nm. The decrease in *d* values indicates a decrease in the amorphous nature attributed to the less oxygen-containing groups [23].

The CQDs prepared from watermelon juice at 3 s and 130°C were also used for the following characterization. TEM images of CQDs are shown in Figure 2a, the as-prepared CQDs are well dispersed, and the selected area electron diffraction (SAED) pattern is shown in the inset. The rings correspond to the {100} {111} {220} {311} planes, which present both graphite- and diamond-like structures [18]. A high-resolution TEM (HRTEM) image in Figure 2b shows

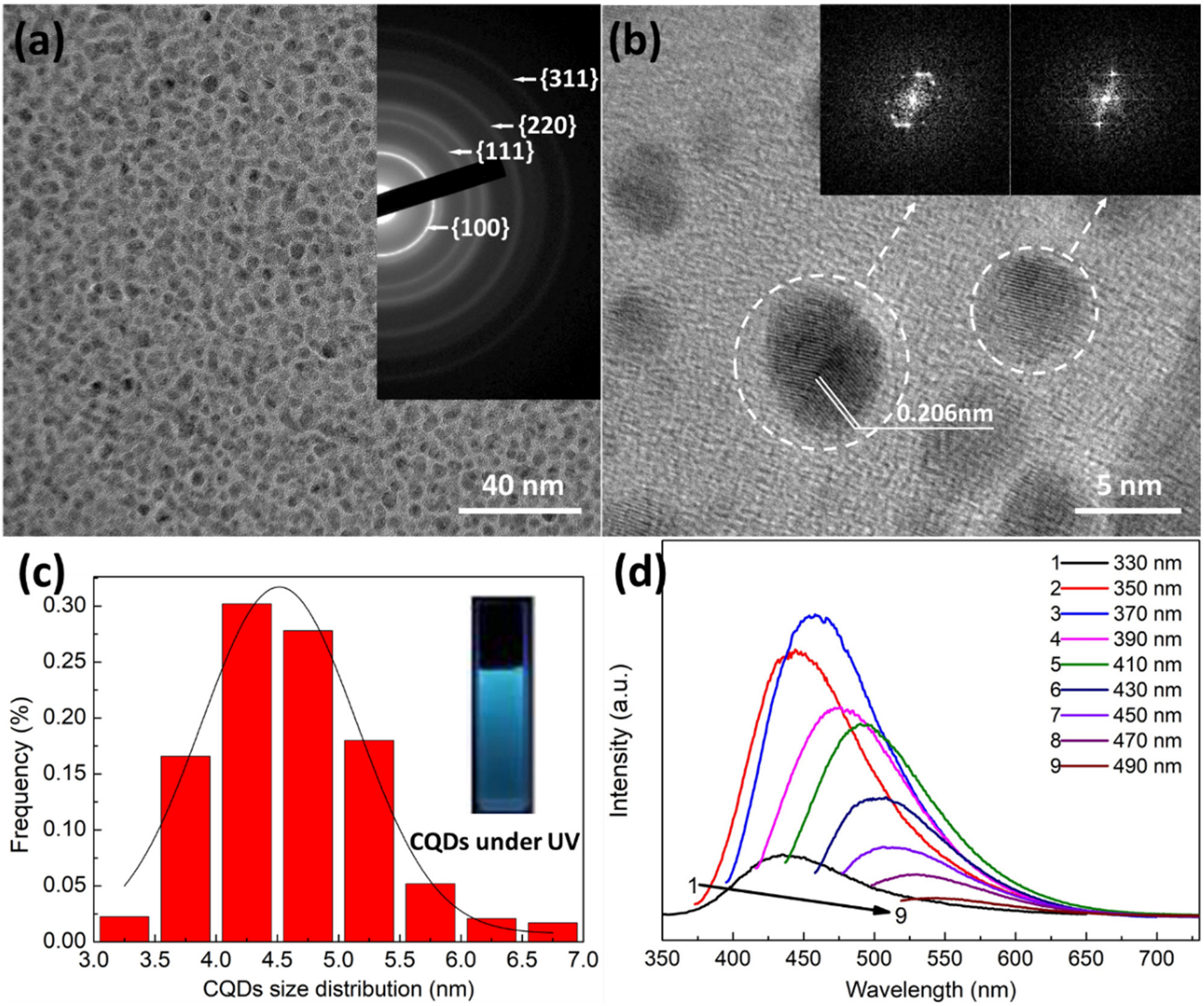

Figure 2: Representative TEM images and fluorescence spectra of CQDs synthesized for 3 s at 130°C, along with direct photographs of the suspension under a 365 nm UV lamp. (a) TEM image of CQDs; the inset is the SAED pattern of CQDs; (b) HRTEM image of CQDs' the insets are the FFT pattern of highlighted areas; (c) the size distribution of CQDs and direct photograph of sample A under a 365 nm UV lamp; and (d) emission profiles at different excitation wavelengths (λ_{ex} = 330–490 nm) recorded for CQDs.

that most of the CQDs contain defects, and the lattice spacing observed varies from 0.20 to 0.23 nm. The fast Fourier transform (FFT) patterns of representative CQDs are displayed in Figure 2b. The observed hexagonal lattices in the FFT image reveal that the CQDs are crystalline hexagonal structures [24]. The size distribution of the CQDs is in a narrow range, 3–7 nm, and is shown in Figure 2c along with the maximum values of the fitted Gaussian peak. The photographs illustrate that the as-prepared CQD suspension shows a blue color under irradiation with a 365 nm ultraviolet (UV) lamp (inset in Figure 2c), suggesting the luminescence nature. Figure 2d presents the PL spectrum, which shows, with the excitation wavelength ranging from 330 to 490 nm, that the emission wavelength changes from 440 to 550 nm. The excitation-dependent emission is mainly caused by surface defects [25]. The blue PL (excited at 370 nm) intensity is much stronger than the green PL (excited at 410 nm) value. Using quinine sulfate as the reference, the quantum yield (QY) of the obtained CQDs was calculated as 42.97% (Figure A3a).

The analytical characterization reveals even more mechanistic insight. The long duration allows a smooth stepwise seed formation and growth of the seed nanodots (Figure A2). As shown in FT-IR spectra, the sucrose molecules in the watermelon juice quickly decompose into small molecules with carboxyl groups in the steam atmosphere. Subsequently, soluble polymers and aromatic rings are generated under the synergistic activation of high temperatures and by hydronium ions. When the concentration of the aromatic clusters reaches a critical supersaturation point, a burst nucleation takes place, and then π-domain-conjugated and surface-defected CQDs are formed. The narrow internal space of the microchannel not only enhances the collision opportunities for the precursors (transport intensification) but also works in unusual process windows and superheated processing (chemical intensification). Meanwhile, the CFD simulation paved the ground for a robust and efficient process. The key to a high-quality CQD nanoproduct is knowledge and control of the pressure and velocity profiles in the microchannel.

3.3 Fluorescence and spectrophotometric detection of NO_2^-

The selectivity and sensitivity of CQDs for NO_2^- detection were evaluated to explore the feasibility of CQDs in environmental applications. Fluorescence screening experiments were performed to identify potential ions that interfere with NO_2^- in the CQD aqueous solution, including Na^+, Co^{2+}, Ni^{2+}, Hg^{2+}, Cu^{2+}, Zn^{2+}, Fe^{3+}, Cr^{3+}, F^-, Cl^-, Br^-, I^-, NO_3^-, CO_3^{2-}, SO_4^{2-}, and PO_4^{3-} (note that the same mechanism is followed for both fluorescence and spectrophotometric readout and representative interferences study for only fluorescent readout was recorded). All results complied with the same conditions (10 μM ions' concentration, excited at 370 nm, and equilibrated for 10 min). As shown in Figure A3b,

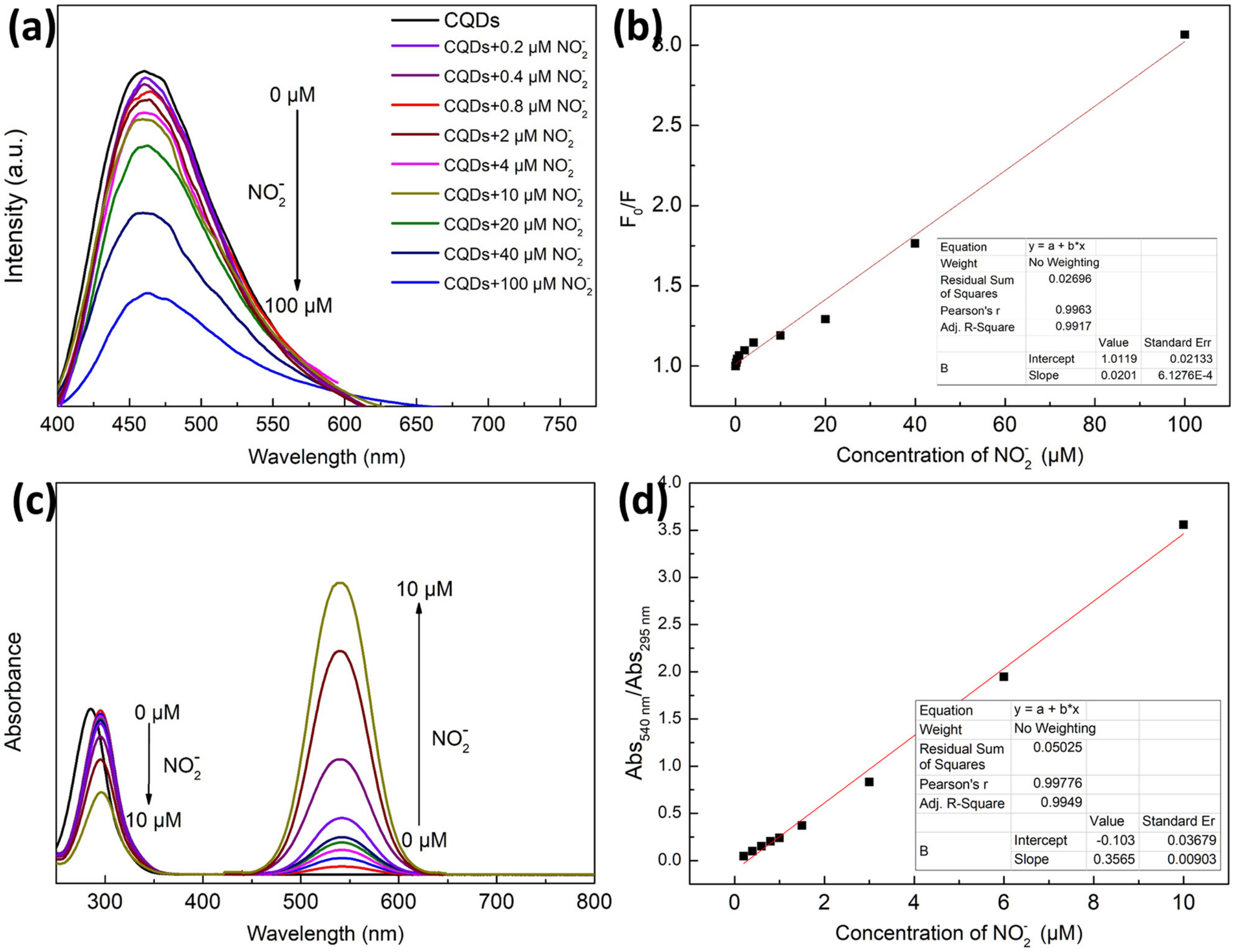

Figure 3: (a) Fluorescence emission spectra of the CQD solution in the presence of different concentrations of NO_2^- (0–100 μM); (b) the linear relationship between F_0/F and NO_2^- concentration; (c) UV-Vis spectra of the CQD solution in the presence of different concentrations of NO_2^- (0–10 μM); and (d) the linear relationship between $Abs_{540\ nm}/Abs_{295\ nm}$ and NO_2^- concentration.

Table 2: Comparison of performances of different methods for the detection of nitrite

Materials	Detection method	Detection wavelength (nm)	Linear range (μM)	LOD (μM)	Ref.
N-CDs	Fluorometry and spectrophotometry	600 and 525, 402	2–60 and 2–80	0.35, 0.13	[8]
CQDs-3-Aph	Fluorometry and spectrophotometry	390 and 440	0.01–0.1 and 2.5–100	0.01, 2.5	[9]
C-dots-NR	Fluorometry and spectrophotometry	520 and 517	0–4.34 and 0–2.9	0.518, 0.196	[26]
CQDs	Fluorometry and spectrophotometry	470 and 295, 540	0.2–100 and 0.2–10	0.11, 0.08	This work

only NO_2^- ions significantly reduced the fluorescence intensity at 470 nm of CQDs (quenching 55% of the blank case at 370 nm); the signal was slightly changed for the remaining ions. This result indicates that CQDs have excellent selectivity for NO_2^- detection.

For sensitivity studies, fluorescence detection and spectrophotometric detection were both performed to assess the response of CQDs to different NO_2^- concentrations. As shown in Figure 3a, a gradual decrease of PL intensity at ~470 nm is observed with the increase of NO_2^- concentrations from 0 to 100 μM. Figure 3b shows a good linear response between F_0/F (where F_0 and F are the PL intensity of CQDs at 470 nm in the absence and presence of NO_2^-, respectively) and the NO_2^- concentration in the range of 0.2–100 μM ($R^2 = 0.9917$). The limit of detection (LOD) for NO_2^- was calculated approximately to be 0.11 μM ($S/N = 3$).

With increasing NO_2^- concentrations from 0 μM to 10 mM, the peak intensity at ~290 nm decreased, while the peak at 540 nm became stronger (Figure 3c). A good linear correlation between the absorbance (ratio values of two absorbance bands ($Abs_{540\ nm}/Abs_{295\ nm}$)) and the concentrations of NO_2^- can be obtained in the concentration range of 2–80 μM (Figure 3d). The LOD was estimated to be 80 nM. In addition, the detection performance of the obtained CQDs was compared with the previously reported CDs in monitoring NO_2^- (Table 2).

3.4 Possible mechanism of NO_2^- quenching the fluorescence of CQDs

As demonstrated in Figures 1b and 3c, a narrow band appears on the CQD curve at 285 nm, which redshifts to 295 nm with the addition of NO_2^-. Due to the p–π conjugation effect of electrons provided by NO_2^- and π electrons provided by CQDs, the $\pi \rightarrow \pi^*$ transition energy decreases, and the absorption peak of the chromophore shifts to the long wave, indicating that NO_2^- might have interacted with CQDs to form the new complex [8]. To confirm this, DLS measurements of CQDs with/without NO_2^- were carried out, as shown in Figure 4a. The average hydrodynamic diameter of CQDs increased from 9 ± 3 to 52 ± 34 nm after the addition of NO_2^-. Moreover, the average lifetime of CQDs (4.57 ± 0.15 ns) was almost the same as that of CQDs + NO_2^- (4.72 ± 0.12 ns), as shown in Figure 4b. Therefore, the mechanism of the optical response of CQDs to

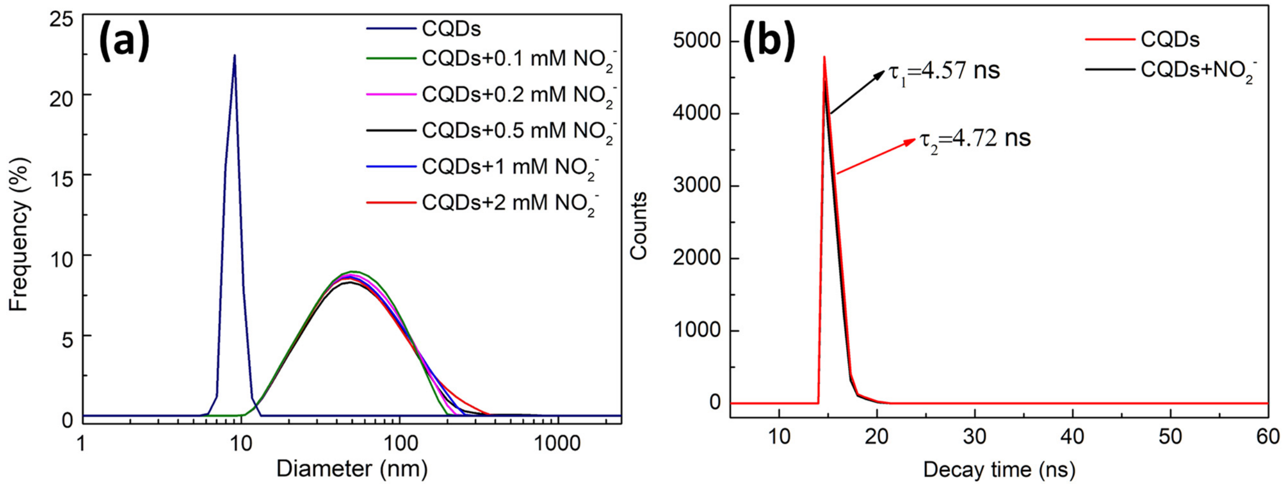

Figure 4: (a) DLS measurements of CQDs with different concentrations of NO_2^-; (b) Fluorescence decay traces of CQDs in the absence (red curve) and presence (black curve) of NO_2^-.

NO_2^- should be attributed to static quenching from NO_2^--induced aggregation of CQDs.

4 Conclusions

Luminescent CQDs were prepared from watermelon juice by a microfluidic steam-based technique, in a chemical reagent-free, time-saving, and continuous manner. Complementary characterization studies revealed that CQDs have a crystalline structure and different functional groups on their surface. The formation mechanism of CQDs was studied through CFD and experiment analysis. In addition, since the addition of NO_2^- to the CQD solution would lead to fluorescence quenching, CQDs were used as probes for NO_2^- detection. Results showed that CQDs possessed a specific response toward NO_2^- both in fluorescence (LOD = 0.11 μM, $S/N = 3$) and spectrophotometric modes (LOD = 0.08 μM, $S/N = 3$). Thus, an effective and simple method was developed for NO_2^- detection using fluorescent CQDs, which holds great promise for practical application in environmental analysis.

Funding information: The authors greatly appreciate the funding support from the National Natural Science Foundation of China (52004102, 22078125), China Postdoctoral Science Foundation (2021M690068), the Fundamental Research Funds for the Central Universities (JUSRP221018, JUSRP622038), and Key Laboratory of Cosmetic Safety Assessment, National Medical Products Administration, Guangdong Institute for Drug Control (KF2021014).

Author contributions: Xiangmiao Zhu: writing – original draft (lead), conceptualization (equal), software (lead), formal analysis (lead), investigation (lead); Weitong Qi: data curation (supporting), formal analysis (supporting); Mi Wang: investigation (supporting), methodology (supporting); Shixuan Zhan: data curation (supporting), investigation (supporting); Xuezhao Liu: methodology (supporting), software (supporting); Yuting Zhao: data curation (supporting), formal analysis (supporting); Volker Hessel: writing – review and editing (equal), resources (supporting), validation (supporting); Zhanghao Chen: investigation (supporting), resources (supporting); Liangliang Lin: conceptualization (equal), Funding acquisition (lead), project administration (lead), resources (lead), supervision (lead), writing – review and editing (equal).

Conflict of interest: Liangliang Lin is a member of the Editorial Board of Green Processing and Synthesis, while Volker Hessel is the Editor-in-Chief of Green Processing and Synthesis.

Data availability statement: The data that support the findings of this study are available from the corresponding author upon reasonable request.

References

[1] Okabe K, Inada N, Gota C. Intracellular temperature mapping with a fluorescent polymeric thermometer and fluorescence lifetime imaging microscopy. Nat Commun. 2012;3(1):1–9. doi: 10.1038/ncomms1714.
[2] Sun YP, Zhou B, Lin Y. Quantum-sized carbon dots for bright and colorful photoluminescence. J Am Chem Soc. 2006;128(24):7756–7. doi: 10.1021/ja062677d.
[3] Li Y, Bai G, Zeng S, Hao J. Theranostic carbon dots with innovative NIR-II emission for in vivo renal-excreted optical imaging and photothermal therapy. ACS Appl Mater Interfaces. 2019;11(5):4737–44. doi: 10.1021/acsami.8b14877.
[4] Lu M, Duan Y, Song Y. Green preparation of versatile nitrogen-doped carbon quantum dots from watermelon juice for cell imaging, detection of Fe3+ ions and cysteine, and optical thermometry. J Mol Liq. 2018;269:766–74. doi: 10.1016/j.molliq.2018.08.101.
[5] Yu BY, Kwak SY. Carbon quantum dots embedded with mesoporous hematite nanospheres as efficient visible light-active photocatalysts. J Mater Chem. 2012;22(17):8345–53. doi: 10.1039/C2JM16931B.
[6] Aziz KHH, Omer KM, Hamarawf RF. Lowering the detection limit towards nanomolar mercury ion detection via surface modification of N-doped carbon quantum dots. N J Chem. 2019;43(22):8677–83. doi: 10.1039/C9NJ01333D.
[7] Omer KM, Aziz KHH, Salih YM. Photoluminescence enhancement via microwave irradiation of carbon quantum dots derived from solvothermal synthesis of l-arginine. N J Chem. 2019;43(2):689–95. doi: 10.1039/C8NJ04788J.
[8] Jia J, Lu W, Li L, Gao Y, Jiao Y, Han H. Orange-emitting N-doped carbon dots as fluorescent and colorimetric dual-mode probes for nitrite detection and cellular imaging. J Mater Chem B. 2020;8(10):2123–7. doi: 10.1039/C9TB02934F.
[9] Wu H, Shen X, Huo D, Ma Y. Fluorescent and colorimetric dual-readout sensor based on Griess assay for nitrite detection. Spectrochim Acta A. 2020;225:117470. doi: 10.1016/j.saa.2019.117470.
[10] Pho QH, Lin L, Tran NN, Tran TT, Nguyen AH, Hessel V. Rational design for the microplasma synthesis from vitamin B9 to N-doped carbon quantum dots towards selected applications. Carbon. 2022;198:22–33. doi: 10.1016/j.carbon.2022.07.004.
[11] Pho QH, Lin L, Rebrov EV, Sarafraz MM, Tran TT, Hessel V. Process intensification for gram-scale synthesis of N-doped carbon quantum dots immersing a microplasma jet in a gas-liquid reactor. Chem Eng J. 2023;452:139164. doi: 10.1016/j.cej.2022.139164.
[12] Hou Q, Xue C, Li N. Self-assembly carbon dots for powerful solar water evaporation. Carbon. 2019;149:556–63. doi: 10.1016/j.carbon.2019.04.083.

[13] Plutschack MB, Pieber B, Gilmore K. The hitchhiker's guide to flow chemistry. Chem Rev. 2017;117(18):11796–893. doi: 10.1021/acs.chemrev.7b00183.

[14] Hartman RLM, Jensen KF. Deciding whether to go with the flow: Evaluating the merits of flow reactors for synthesis. Angew Chem Int Ed. 2011;50:7502–19. doi: 10.1002/anie.201004637.

[15] Paul EL, Atiemo-Obeng VA, Kresta SM. Handbook of industrial mixing: science and practice. New Jersey, US: John Wiley & Sons; 2004. p. 99–103. doi: 10.1002/0471451452.

[16] Avila KM, de Lozar A, Avila M. The onset of turbulence in pipe flow. Science. 2011;333:192–6. doi: 10.1126/science.1203223.

[17] Batchelor GK. An introduction to fluid dynamics. Cambridge: Cambridge University Press; 2000. p. 156.

[18] Li X, Zhang S, Kulinich SA. Engineering surface states of carbon dots to achieve controllable luminescence for solid-luminescent composites and sensitive Be2+ detection. Sci Rep-UK. 2014;4(1):1–8. doi: 10.1038/srep04976.

[19] Hu SL, Niu KY, Sun J. One-step synthesis of fluorescent carbon nanoparticles by laser irradiation. J Mater Chem. 2009;19(4):484–8. doi: 10.1039/B812943F.

[20] Zhu S, Zhang J, Tang S. Surface chemistry routes to modulate the photoluminescence of graphene quantum dots: from fluorescence mechanism to up-conversion bioimaging applications. Adv Funct Mater. 2012;22(22):4732–40. doi: 10.1002/adfm.201201499.

[21] Hsu PC, Shih ZY, Lee CH. Synthesis and analytical applications of photoluminescent carbon nanodots. Green Chem. 2012;14(4):917–20. doi: 10.1039/C2GC16451E.

[22] Baker SN. Luminescent carbon nanodots: emergent nanolights. Angew Chem Int Ed Engl. 2010;49(38):6726–44. doi: 10.1002/anie.200906623.

[23] Peng J, Gao W, Gupta BK. Graphene quantum dots derived from carbon fibers. Nano Lett. 2012;12(2):844–9. doi: 10.1021/nl2038979.

[24] Ye R, Xiang C, Lin J. Coal as an abundant source of graphene quantum dots. Nat Commun. 2013;4(1):2943. doi: 10.1038/ncomms3943.

[25] Cayuela A, Soriano ML, Carrillo-Carrión C, Valcárcel M. Semiconductor and carbon-based fluorescent nanodots: the need for consistency. Chem Commun. 2016;52(7):1311–26. doi: 10.1039/C5CC07754K.

[26] Hu X, Shi J, Shi Y, Zou X, Tahir HE, Holmes M. A dual-mode sensor for colorimetric and fluorescent detection of nitrite in hams based on carbon dots-neutral red system. Meat Sci. 2019;147:127–34. doi: 10.1016/j.meatsci.2018.09.006.

Appendix

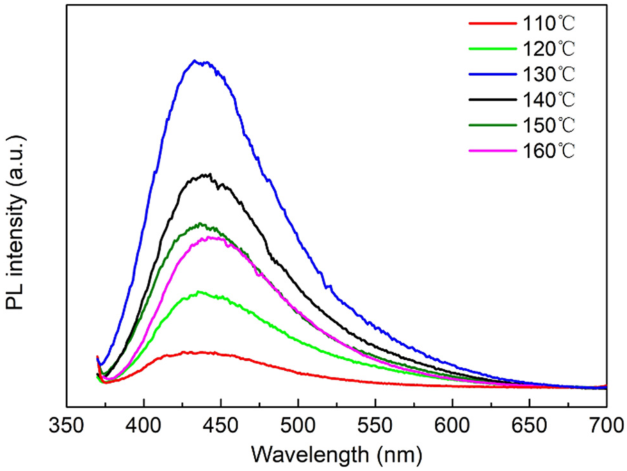

Figure A1: The fluorescence spectra of CQDs prepared from watermelon juice by the microfluidic method for 3 s at different temperatures.

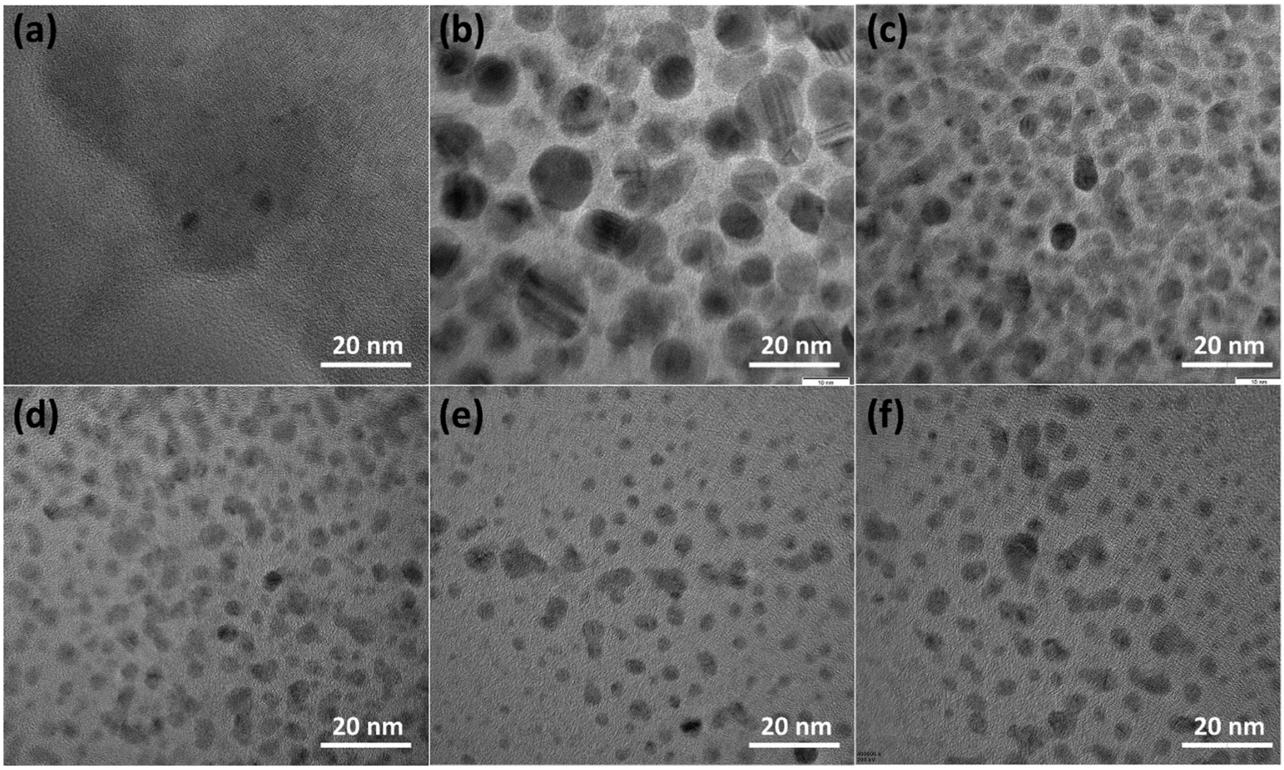

Figure A2: TEM images of CQDs prepared from watermelon juice by the microfluidic method for in 3 s at different temperatures: (a) 110°C, (b) 120°C, (c) 130°C, (d) 140°C, (e) 150°C, and (f) 160°C.

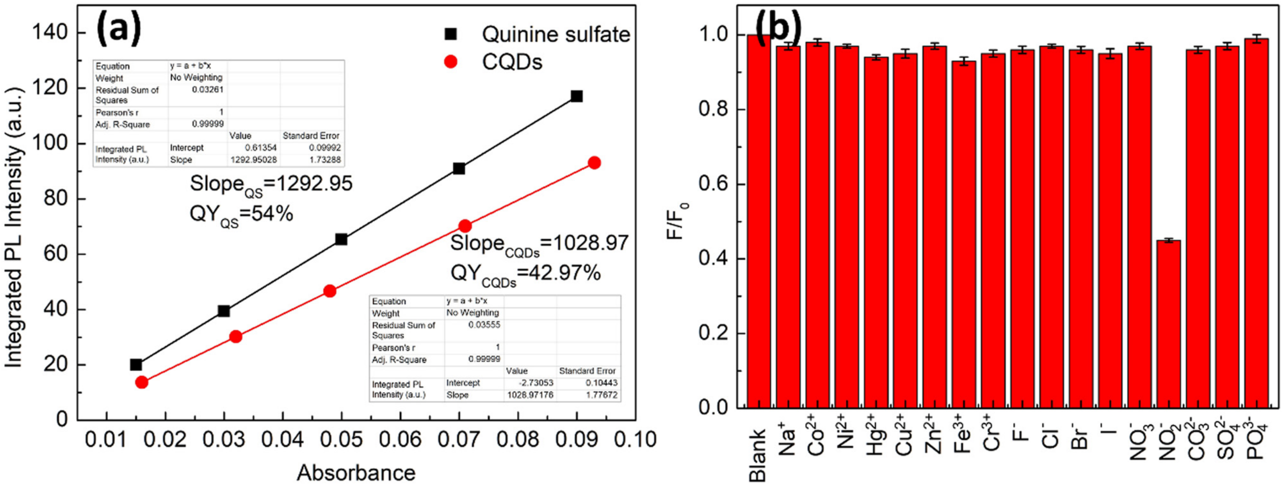

Equation	y = a + b*x		
Weight	No Weighting		
Residual Sum of Squares	0.03261		
Pearson's r	1		
Adj. R-Square	0.99999		
		Value	Standard Error
Integrated PL Intensity (a.u.)	Intercept	0.61354	0.09992
	Slope	1292.95028	1.73288

Equation	y = a + b*x		
Weight	No Weighting		
Residual Sum of Squares	0.03555		
Pearson's r	1		
Adj. R-Square	0.99999		
		Value	Standard Error
Integrated PL Intensity (a.u.)	Intercept	-2.73053	0.10443
	Slope	1028.97176	1.77672

Figure A3: (a) Plots of integrated PL intensity against absorbance of quinine sulfate and CQDs at λ_{ex} = 370 nm. (b) Fluorescence response of the CQD aqueous solution in the presence of different ions at λ_{em} = 470 nm.

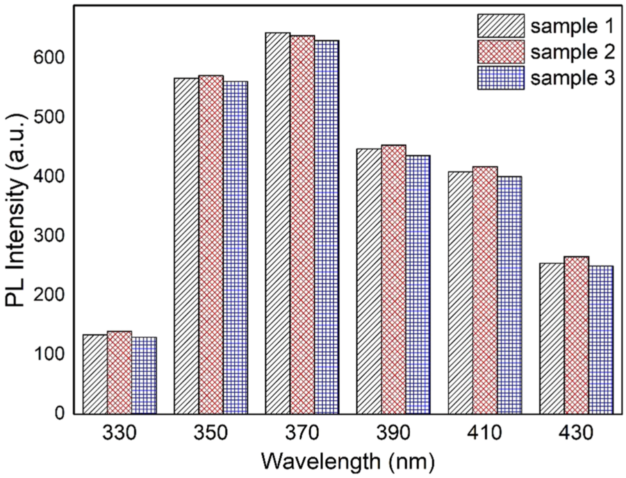

Figure A4: The maximum PL intensity (excited with different excitation wavelengths) of the three samples, all synthesized at 130°C for 3 s.